



# Additive manufacturing of aluminum Al 6061 alloy using metal injection molding granules: green density, surface roughness, and tomography study

Swathi K.Manchili<sup>1,2</sup> · Gurminder Singh<sup>1,3</sup> · Jean-Michel Missiaen<sup>1</sup> · Didier Bouvard<sup>1</sup>

Received: 10 May 2024 / Accepted: 2 September 2024  
© The Author(s), under exclusive licence to Springer Nature Switzerland AG 2024

## Abstract

In the present study, a metal injection molding (MIM) feedstock of aluminum Al 6061 was used as the raw material for extrusion 3D printing and sintering-based AM. A design of experiments methodology was used to systematically analyze the individual and interactive effects of various parameters, such as extrusion temperature, extrusion flow rate multiplier, nozzle printing speed on the green density, and surface roughness. MIM feedstock resulted in shear-thinning behavior as required for extrusion printing. The initial findings revealed a decrease in green density with an increase in nozzle speed, whereas a contrasting trend was observed with a reduction in the extrusion flow rate. A similar trend was observed for the surface roughness measured along the printing direction. Through the application of regression equations and a multi-objective optimization technique, the study achieved the dual objectives of maximizing the green density and minimizing the surface roughness. To comprehensively evaluate the manufactured components, microtomography analysis was conducted on specimens produced under optimized parameters and randomly selected conditions. Subsequently, the specimens underwent debinding and sintering processes to obtain the sintered metal parts. However, sintering results in poor densification, which requires further investigation. The investigations provided valuable insights into optimizing the production of green parts endowed with higher density and better surface characteristics by leveraging extrusion 3D printing of aluminum Al 6061 MIM feedstock.

**Keywords** Extrusion 3d printing · Aluminum · Design of experiments · Optimization · Surface roughness · Additive manufacturing · Metal injection molding · Feedstock

## 1 Introduction

Aluminum (Al) alloys are known for their versatility, strength, cost-effectiveness, aesthetic appeal, and reliability. They have applications in a diverse range, from soft and highly ductile wrapping foils to demanding engineering uses

[1]. These alloys are extensively employed in aerospace, automotive, electronics, construction, and infrastructure applications, owing to their impressive specific strength, excellent processability, and notable thermal and electrical conductivity [2–4]. Aluminum, along with steel, is one of the most widely used materials, offering a density approximately one-third that of steel [5]. Its high specific strength, characterized by a high strength-to-density ratio, facilitates the construction of robust lightweight structures. Various manufacturing processes, including casting, forging, rolling, machining, welding, shearing, and forming, have traditionally been applied to shape aluminum and its alloy components into different forms and designs [6]. However, these conventional processes have limitations in terms of the design flexibility for customized fabrication.

Metal Injection Molding (MIM) has become a pivotal manufacturing method for fabricating intricate geometries using high-performance materials, particularly

---

Swathi K.Manchili and Gurminder Singh are Equal Contributions.

✉ Gurminder Singh  
Gurmindersingh2012@gmail.com;  
Gurminder.singh@iitb.ac.in

<sup>1</sup> University Grenoble Alpes, CNRS, Grenoble INP, SIMAP, 38000 Grenoble, France

<sup>2</sup> Department of Manufacturing Processes, RISE Research Institutes of Sweden AB, Argongatan 30, Mölndal, Sweden

<sup>3</sup> Department of Mechanical Engineering, Indian Institute of Technology Bombay, Mumbai, India

aluminum alloys. In injection molding, the melted polymer is injected into a die to create a final product. In Metal Injection Molding (MIM), a metal and binder composite is injected into a die to form a green part of the product. The green part was then debinded and sintered to achieve the final shape of the product. MIM facilitates the production of complex shape components with superior thermal and electrical conductivity and is a compelling choice for diverse applications, including the manufacture of heat sinks [7, 8]. The MIM process offers precision, high repeatability, speed, and cost-effectiveness per part, and is accompanied by a superior surface finish and a densely structured final product. Nevertheless, the MIM process involves several steps, including injection molding, debinding, and sintering, all of which contribute to higher processing costs. Additionally, creating customized dies for each design in batch production is expensive when creating intricate and unique final shapes. This limitation can be addressed by preparing customized dies through additive manufacturing or directly using MIM feedstock as the raw material for extrusion 3D printing and sinter-based AM. The present manuscript focuses on the second route.

In recent years, the rapid development of metal additive manufacturing (AM) technologies has been particularly advantageous for generating metal parts across numerous industries, owing to their diverse capabilities [9, 10]. Powder-based procedures have been widely employed in AM techniques, including electron beam melting (EBM), selective laser melting (SLM), rapid tooling, and direct energy deposition (DED) for materials, such as titanium alloys, nickel-based alloys, and steels [11–14]. In these processes, metal particles melt directly during scanning using a laser or electron source. These processes can be used to fabricate customized dies for MIM directly. However, the challenges include high costs and difficulty in controlling the fabrication process. Additionally, it is challenging to use these methods with reflective and conductive materials, such as pure aluminum, copper, and silver.

Extensive research has been conducted on AM of aluminum alloys using SLM, including AlSi10Mg, AlSi7Mg, AlSi12, Al<sub>20</sub>Si<sub>5</sub>Fe<sub>3</sub>Cu, AlCuMg, AA-4047, AA-2618, and AA-2024 [15, 16]. Wang et al. [16] studied the effects of the printing orientation and heat treatment on the tensile characteristics of AlSi10Mg prepared by SLM. Yang et al. [17] discussed the microstructure and mechanical characteristics of an Al-5Mg<sub>2</sub>Si-2 Mg alloy fabricated using SLM. These results are promising for achieving defect-free parts. Martin et al. [18] achieved robust Al alloys with nucleant nanoparticles using SLM, challenges such as pore formation, cracks, laser spatter, and shape distortion persist. Moreover, these AM methods are known for their cost, complexity, and reliance on highly skilled labor.

In addition to the above-mentioned AM processes, techniques such as binder jetting (BJ) and fused filament fabrication (FFF) of metal filaments with a combination of pressureless sintering fall under the umbrella of low-cost sinter-based AM technologies [19–24]. In these methodologies, parts are initially formed through AM, such as BJ and FFF utilizing a binder, followed by a sintering process to eliminate the binder and consolidate/densify the material, similar to the Metal Injection Molding (MIM) process. These processes have been developed for different types of materials, such as copper [25], steel [26], Inconel [27], alumina [28], and tungsten carbide [29]. However, these processes have not been extensively explored for the fabrication of aluminum alloys.

Zanon et al. [30] fabricated Al 6061 green parts using BJ with specialized aluminum compatible binder. The samples were printed with 500 layers and later cured using oven at 200 °C for 12 h under nitrogen. Further, samples were debinded at 500 °C and sintered at 625 °C by placing on graphite crucible under tube furnace with nitrogen atmosphere. However, the sintered samples exhibited low hardness, rupture strength, and conductivity values. Yamaguchi and Oya [31] showed the details of sintering and the requirement of a printing strategy for binder jetting of aluminum alloys using in situ X-ray tomography. The binder arrangement with the dispersion settings and printing strategy has a strong influence on the sinterability of aluminum. The parts resulted in insufficient sintered areas owing to the inhomogeneous dispersion of the binders.

For the FFF of aluminum alloys, Malone [32] showed the effect of the process parameters of 3D printing on the surface roughness and porosity of green samples using in-house developed aluminum Al6061 and binder filaments. The sintered samples showed low densities between ~47% and 70% and low hardness values. This could be due to the inappropriate selection of binders and process parameters in the green state, which leads to a poor density. Galindo et al. [33] developed a filament for AlSi10Mg using polylactic acid-based binders. The printed green parts result in porosity in the microscopy images. The sintering of the printed green parts has not been described. Ding et al. [34] developed filament for Al7075 alloys with binders like polyethylene oxide and polypropylene powders. The printed green parts resulted in ~93.2 of ~96.1% relative density after sintering. Momeni et al. [35] prepared filaments for aluminum alloys (graded not provided) using a thermoplastic elastomer as the main binder component and blended them with polypropylene (PP), grafted-maleic anhydride-PP (PPMA), and grafted-maleic anhydride-PPwax (PPMAwax) plus PP binders. An in-depth study of the thermal and rheological properties, as well as the morphology, was performed. The Al/TPE/PP and Al/TPE/PPMA filaments showed good printability. However, Al/TPE/PP/PPMA wax samples displayed considerable

defects and irregularities. These issues were attributed to the reduced viscosity at the high printing temperature of 240 °C and the minimal elongation at break in the Al/TPE/PP/PPMAwax feedstock filament, leading to more instability during the extrusion process. Consequently, the quality of the produced parts is significantly lower. Tang et al. [36] used starch as binder to mix with pure aluminum and organic solvents to print green parts. Solvent evaporation, starch removal, and parameter tuning were used to create hierarchical voids. The developed material exhibits shear-thinning characteristics for 3D printing. Achieving successful slurry filament extrusion and deposition requires modifying variables, such as printing speed, applied air pressure, and nozzle diameter. The aluminum structures were then created by sintering the material for 30 min at 650 °C. Longer holding times resulted in an increase in linear shrinkage as sintering necks of the aluminum particles developed. A feedstock consisting of AA 7429 Al alloy mixed with stearic acid binders, petroleum jelly, and high-density polyethylene was developed by Dayam et al. [37]. An in-house designed plunger-based 3D printing method was used to extrude feedstock paste. The samples were then heated to 250 °C at a rate of 10 °C/min and subjected to thermal debinding at 320 °C. Subsequently, the pieces were sintered for 9 h at 720 °C. The final samples exhibited a tensile strength that was 20% less than that of the wrought alloy and a density of up to 60.67%.

While many researchers have developed in-house feedstocks for extrusion 3D printing and sintering of aluminum alloys, the industry-level applicability of these feedstocks requires comprehensive analysis and repeatability checks. Alternatively, commercially available MIM granular feedstocks can be processed through screw-based extrusion 3D printing, which differs from the conventional filament-based 3D printing, to achieve the desired repeatable properties of aluminum alloys, particularly for high-end industrial applications. The use of screw-based extrusion 3D printing provides advantages over the filament-based extrusion process, such as continuous bulk feeding of the feedstock from the hopper, direct printing of commercially available granular feedstocks, and better mixing during printing [38]. The present author group demonstrated the use of MIM granular feedstock for screw-based extrusion 3D printing (E3DP) of copper and steel [26, 39, 40]. As observed in the literature, the process parameters in the E3DP process were important to optimize to obtain defectless parts in green form, which could result in a higher density after sintering.

The novelty of this study is the use of a commercially available Al6061 MIM granular material for additive manufacturing using extrusion 3D printing and sintering processes. A commercially sourced MIM Al6061 aluminum alloy granular feedstock from Ryer, USA, was used directly in the screw-based E3DP process. Granular feedstock was designed for injection molding. However, because of the

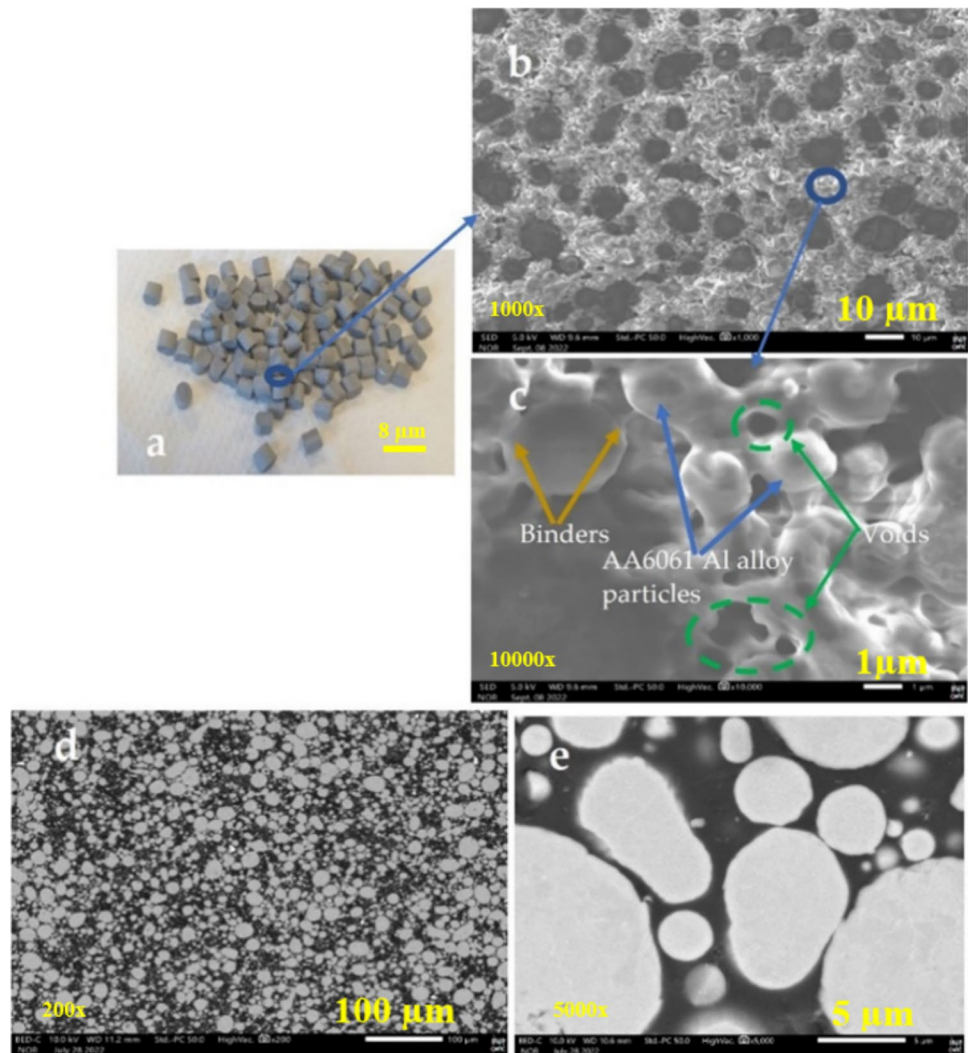
different set of unidentified binders compared to previous studies, optimization of printing parameters is required for defectless parts. However, the use of MIM Al6061 granular feedstock for screw-based E3DP has not yet been explored. A thorough investigation of numerous E3DP parameters was performed to maximize the green density and reduce surface roughness. The utilization of a statistical methodology, namely, the design of experiments (DOE), enabled the development of regression models that exposed the complex correlations between crucial printing parameters, such as extrusion temperature, extrusion multiplier (flow rate), nozzle speed for surface roughness, and density of the green part. Using these models, the parameters were methodically optimized to produce printed components with improved surface roughness and increased green density. Scanning electron microscopy and microtomography were used to visually evaluate the void morphology arising from various printing parameters in both optimal and non-optimized printed samples. Finally, sintering was performed on the specimen that was printed using ideal settings to obtain a consolidated and densified finished part.

## 2 Material and methodology

### 2.1 Material

Commercially sourced Al6061 aluminum alloy MIM granules were acquired from RYER Inc., USA and directly employed as the raw material for extrusion 3D printing. Micrographs of the feedstock granules are shown in Fig. 1. Figure 1 (a) illustrates MIM feedstock granules with dimensions ranging from 4 to 6 mm. The feedstock comprises two types of binders: a solvent-soluble first binder and a second binder that serves as the backbone after removal of the first binder during the debinding step. Both binders contribute to flowability, which is an essential characteristic for material injection into the die, thereby facilitating extrusion printing. Figure 1 (b) and (c) shows scanning electron microscopy (SEM) micrographs of the granule surface at varying magnifications, revealing alloy particles embedded in the binder along with discernible voids. The granules were then placed directly into the SEM equipment. The samples were debinded and impregnated with epoxy resin for polishing for better morphological characterization. The binder-free particles were polished with up to 1200 SiC grit paper along with diamond finishing and placed in an SEM machine for back-scattered scanning. Figure 1 (d) and (e) shows micrographs of the polished cross-section of the feedstock granule, highlighting the spherical morphology of the alloy particles at different magnifications. Comprehensive measurements involving approximately 200 assessments from 10 distinct micrographs of feedstock granule cross-sections indicated

**Fig. 1** (a) MIM feedstock granule of AA6061 Al alloy, (b) and (c) SEM image showing the components, binder, and metal particles, present in the feedstock, (d) SEM image showing the cross-section of the feedstock revealing metal particles, and (e) high magnification BSE image showing the aluminum alloy particles



a particle size range for AA6061 Al alloy particles extending from submicron to approximately 30  $\mu\text{m}$ . The composition of the AA6061 Al alloy, as provided by the seller in Table 1, indicates a feedstock composition comprising 18.5 wt% binders, with specific details regarding the composition of each binder not disclosed by the supplier.

## 2.2 3D printing

Extrusion 3D printing was performed using an ExAM 255 screw-based extrusion 3D printer acquired from AIM3D, Germany, as illustrated in Fig. 2. The printer featured a built-up region of 255 mm in all the three dimensions. Feedstock granules were introduced into the printer hopper, from which

a pneumatic-powered piston (referred to as a faker) continuously and uniformly pushed the feedstock into the extruder. A cooling jacket with both channels was strategically positioned near the extruder heater after the beaker to prevent feedstock jamming. This cooling jacket facilitated the melting of the binder before it reached the extrusion nozzle, thus mitigating issues related to temperature gradients. The extruder was equipped with a 0.4 mm-diameter nozzle made of hardened steel to reduce nozzle wear caused by metal particles during printing. The extruder was maintained at a controlled temperature, termed the extrusion temperature, to ensure uniform extrusion. The shapes for printing were modeled using SolidWorks software, saved as binary tessellation files (STL), and imported into Simplify3D for slicing.

**Table 1** Composition of AA6061 Al alloy (provided by the vendor)

Element	Al	Cr	Cu	Fe	Mg	Mn	Si	Ti	Zn
Percentage composition	Balance	0.15	0.21	0.11	0.93	0.01	0.47	0.01	0.01

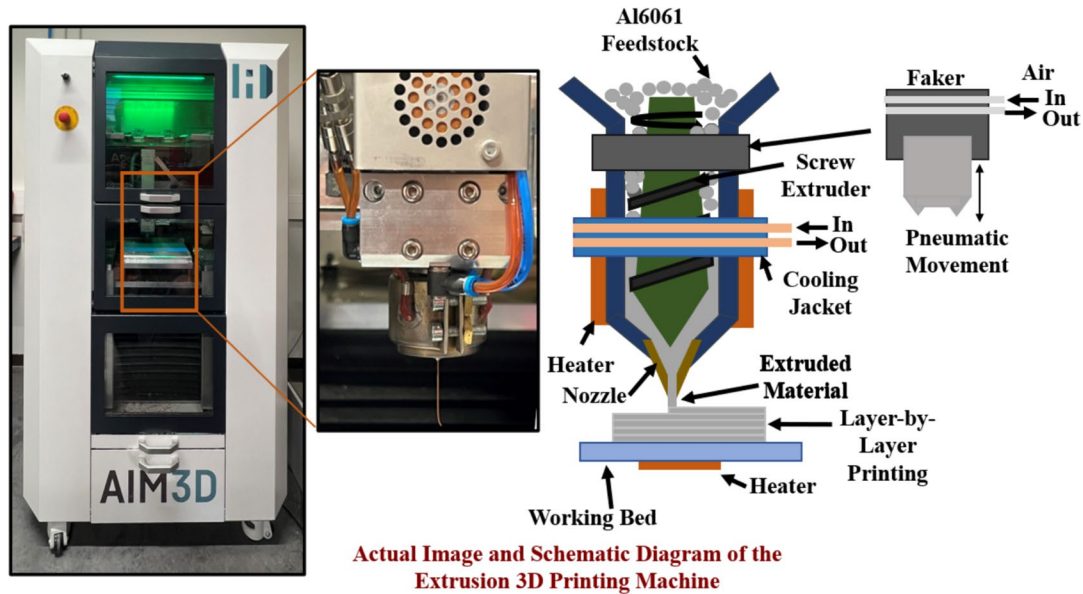


**Fig. 2** Screw-based extrusion 3D printer with MIM feedstock

**Table 2** Printing parameters for CCD RSM

Serial no	Parameters	-1	0	1
1	Extrusion temperature ( °C)	195	200	205
2	Extrusion multiplier (%)	100	120	140
3	Nozzle speed (mm/s)	20	30	40

Cylindrical samples, 8 mm in length and 8 mm in diameter, were used as specimens in the present study. A consistent infill density of 100% was selected to generate dense pieces. The layer thickness was fixed at 0.05 mm. An offset of  $\pm 45^\circ$  is used in each layer of the rectilinear infill pattern. During the printing process, the bed temperature was maintained at 60 °C, a setting that was chosen with concern for wrapping flaws and first layer collapse. With emphasis on surface roughness and green density, a design of experiments was used to examine the effects of changing the nozzle speed, extrusion multiplier (normalized flow rate), and extrusion temperature on the printing performance (see Sect. 2.5 and Table 2). The generated toolpath was saved as a G-code output for the interaction with the printer.

### 2.3 Debinding and sintering

The debinding procedure was performed in two consecutive steps to remove the primary and secondary binders from the samples. The samples were submerged in acetone at 50 °C for 16 h as a part of the solvent debinding stage, which was initially designed to remove the primary binder. Following

solvent debinding, the samples were dried in preparation for subsequent thermal debinding.

Thermal debinding and sintering processes were performed under a steady flow of pure nitrogen in a vertical dilatometer, as the feedstock provider Ryer recommended and are typically used for sintering MIM Al alloys [7, 41]. To remove binders, the sample was first heated to 425 °C at a 1 °C/min rate and maintained at this temperature for an hour. The debinding cycle was assessed by preliminary thermogravimetric analysis. The temperature was then increased from the debinding temperature to 625 °C at a rate of 4 °C/min. After maintaining the sintering temperature for an hour, the samples were cooled to room temperature at a rate of 4 °C/min. The debinding and sintering cycles were carefully regulated to match the properties of the MIM granules used in the procedure.

### 2.4 Characterizations

Rheological properties of the feedstock were evaluated using an MCR 302 rheometer (Anton Paar, Austria). The measurements were taken with a parallel plate setup (25 mm diameter, 0.5 mm gap between plates). After printing, the green densities of the samples were determined by calculating their mass and volume. A fine balance with an accuracy of 0.001 g was used to determine the mass and a Vernier caliper was used to calculate the volume from the dimensions. Each sample was measured three times, and the results are shown as the averages of these readings. The surface roughness of the green samples was measured using an Olympus DSX510

**Table 3** Responses and input parameters for 3D printing

Trail No	Extrusion temperature (°C)	Extrusion multiplier (%)	Nozzle speed (mm/s)	Surface roughness (μm)	Green density (g/cc)
1	195	140	20	8.50	1.84
2	200	140	40	8.90	1.85
3	195	100	20	13.97	1.79
4	205	140	40	12.70	1.83
5	200	120	30	9.30	1.85
6	195	100	30	14.78	1.77
7	205	100	40	15.48	1.79
8	200	100	30	11.70	1.82
9	195	120	40	13.23	1.76
10	205	140	30	10.90	1.86
11	205	120	40	13.63	1.82
12	195	120	20	9.570	1.81
13	195	140	30	10.90	1.80
14	195	100	40	16.16	1.74
15	200	120	20	8.60	1.86
16	205	100	20	11.30	1.84
17	205	100	30	12.10	1.81
18	205	140	20	8.59	1.88
19	200	140	20	7.50	1.90
20	195	140	40	10.51	1.78
21	200	100	20	10.43	1.85
22	200	120	40	10.33	1.83
23	195	120	30	11.08	1.79
24	200	100	40	12.53	1.81
25	205	120	20	9.57	1.85
26	205	120	30	11.39	1.83
27	200	140	30	7.84	1.87

optical microscope (Tokyo, Japan) in accordance with ISO 21920–2 [42]. Surface profiles were acquired along the printing direction. A JEOL JSM-IT 500 HR microscope (Japan) was used for the study of scanning electron microscopy.

To comprehensively examine the internal structure, 3D scanning was conducted using an Easytom XL computed microtomography machine (France) with an energy level of 110 kV and a voxel size of 2.2 μm. A 360° rotation around the vertical axis was executed to capture projections, and subsequent image reconstruction was performed using the Phoenix built-in software. Post-processing analysis was performed using ImageJ and the Avizo Lite software. ImageJ facilitated the importation of tomographic images, followed by thresholding to isolate pores within

the sample. A three-dimensional (3D) connection technique, as detailed by Boulos et al. [18], was utilized for segmentation, enabling measurements of pore volume, pore surface area, equivalent diameter, and sphericity. Visualization of the pores and samples was accomplished using the Avizo Lite software.

## 2.5 Design of experiments

As indicated in Table 2, a full-factorial design-based design of experiment (DOE) approach was used to evaluate the effects of three variables—extrusion temperature, extrusion flow rate multiplier, and nozzle printing

speed—on the observed responses (surface roughness and green density). SAS Institute's JMP 7 program (Cary, North Carolina, USA) was used to analyze the data. The machine capabilities and outcomes of the preliminary testing were considered to obtain the ranges of the nozzle speed, extrusion multiplier, and extrusion temperature. A few pilot experiments were conducted to finalize the range and levels of the values for the printing parameters. Samples printed with lower than extrusion temperature of 195 °C, extrusion multiplier of 100%, nozzle speed of 20 mm/s and higher than extrusion temperature of 205 °C, extrusion multiplier of 140%, and nozzle speed of 40 mm/s were resulted in large defects such as poor surface finish and voids tested by visual inspection. Therefore, three levels were assigned to each of the three factors, whose experimental values were as follows: (1) extrusion multipliers of 100, 120, or 140%; (2) nozzle speeds of 20, 30, or 40 mm/s; and (3) extrusion temperatures of 195 °C, 200 °C, and 205 °C. The 27 printing trials were conducted using this experimental design, as shown in Table 3. Three samples were fabricated for each printing trial. The surface roughness and green density were measured for all samples. The average of the measurements from the three samples was used for regression analysis.

### 3 Results and discussion

#### 3.1 Design of experiment analysis

According to the DOE, 27 experiments were conducted, and Table 3 lists the measured average surface roughness and green component density. An analysis of variance and response surface methodology were used to examine the effects of the parameters on the responses. Regression models were developed, and are provided in Eqs. 1 and 2, respectively. Figure 3 shows the fit of the regression models to the experimental values. The generated models were significant, with p values less than 0.05, and the R<sup>2</sup> values for the roughness value and green component density were 72% and 74%, respectively. In addition to the DOE table, multiple random sets of experiments were conducted within specified constraints to validate the models. The outcomes of these experiments were closely aligned with the predictions made by the regression models.

Green Density: 1.8237037037

$$\begin{aligned}
 &+ 0.0238888889 \cdot \left( \frac{(Extrusion\ Temperature - 200)}{5} \right) \\
 &+ 0.0222222222 \cdot \left( \frac{(Extrusion\ Multiplier - 120)}{20} \right) \\
 &+ -0.0233333333 \cdot \left( \frac{(Nozzle\ Speed - 30)}{10} \right) \\
 &+ \left( \frac{(Extrusion\ Temperature - 200)}{5} \right) \cdot \left( \frac{(Extrusion\ Multiplier - 120)}{20} \right) \cdot 0.0008333333 \\
 &+ \left( \frac{(Extrusion\ Temperature - 200)}{5} \right) \cdot \left( \frac{(Nozzle\ Speed - 30)}{10} \right) \cdot 0.0025 \\
 &+ \left( \frac{(Extrusion\ Multiplier - 120)}{20} \right) \cdot \left( \frac{(Nozzle\ Speed - 30)}{10} \right) \cdot -0.0025
 \end{aligned} \tag{1}$$

Surface Roughness: 11.166296296

$$\begin{aligned}
 &+ -0.168888889 \cdot \left( \frac{(Extrusion\ Temperature - 200)}{5} \right) \\
 &+ -1.783888889 \cdot \left( \frac{(Extrusion\ Multiplier - 120)}{20} \right) \\
 &+ 1.4133333333 \cdot \left( \frac{(Nozzle\ Speed - 30)}{10} \right) \\
 &+ \left( \frac{(Extrusion\ Temperature - 200)}{5} \right) \cdot \left( \frac{(Extrusion\ Multiplier - 120)}{20} \right) \cdot 0.06925 \\
 &+ \left( \frac{(Extrusion\ Temperature - 200)}{5} \right) \cdot \left( \frac{(Nozzle\ Speed - 30)}{10} \right) \cdot 0.3741666667 \\
 &+ \left( \frac{(Extrusion\ Multiplier - 120)}{20} \right) \cdot \left( \frac{(Nozzle\ Speed - 30)}{10} \right) \cdot -0.0791666667
 \end{aligned} \tag{2}$$

#### 3.2 Influence of printing parameters on green density

The influence of the factors on green density is depicted in Fig. 4, which also shows the percentage contribution of each term and how they interact. All trials had relative green densities between 1.73 and 1.9 g/cc, with the extrusion multiplier being the most important factor. Interestingly, there were no discernible interactions between the parameters of green diversity. The impact of these parameters on the green density is thoroughly discussed below.

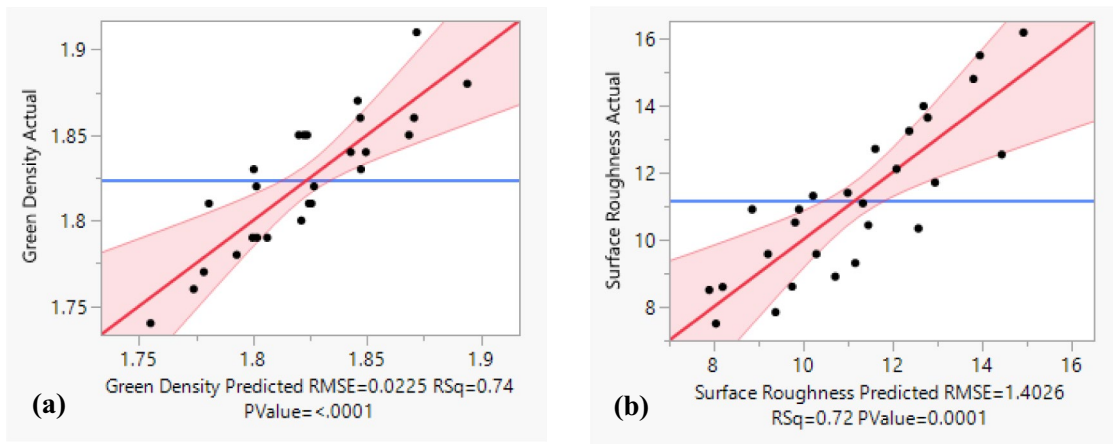


**Fig. 3** Actual vs predicted graph for (a) green density and (b) surface roughness

### 3.2.1 Effect of extrusion temperature

Throughout the extrusion printing process, the feedstock undergoes various stresses in the feeder, screw extruder, and nozzle, and squeezes the filament on the previously printed material. These stresses can potentially damage the material, leading to the formation of voids. Two types of voids were identified: voids within the feedstock material and voids observed between the printed filaments in the resulting samples. The chosen printing parameters influence the presence of these voids, and their minimization is essential for achieving a higher green density.

As for the extrusion temperatures (195, 200, and 205 °C), Fig. 4 illustrates a trend in which the green density initially increases and then decreases with increasing temperature. The initial increase in the green density was attributed to the decreased viscosity of the feedstock material, rendering it more deformable. Lower temperatures resulted in the formation of numerous voids (Fig. 5(a)), whereas higher temperatures led to a reduction in voids (Fig. 5(b)). However, a further increase in the extrusion temperature beyond a certain point resulted in a decline in the green density owing to binder degradation, leading to increased voids (Fig. 5(c)). The binder composition of the feedstock used is unknown (not provided by the vendor). Therefore, the assessment of binder degradation was approximated using visual inspection as a qualitative approach. Consequently, the samples extruded at 200 °C exhibited the most favorable green density. This observation was consistent with the findings of Singh et al. [19]. They noted a similar behavior in the extrusion printing of copper MIM feedstock. As the temperature approached the degradation point of the binder, the breakdown during printing led to void formation. This behavior is particularly crucial in MIM feedstock extrusion printing, given the high weight percentage of the metal particles present. A rheological study of the Al 6061 MIM feedstock at

200 °C (Fig. 6) revealed shear-thinning behavior, which is essential for the extrusion 3D printing process [43, 44].

### 3.2.2 Effect of extrusion multiplier

The extrusion multiplier has emerged as a critical factor that significantly influences the morphology of the extruded material. A direct relationship was observed; as the extrusion multiplier increased, the green density also increased. This relationship can be attributed to the increased flow rate associated with an increased extrusion multiplier. The flow rate, which represents the amount of material deposited, leads to the formation of smaller extrusion and printing voids, thereby fostering improved adhesion with the underlying layer. Consequently, SEM micrographs (Fig. 7) demonstrated that higher extrusion multipliers resulted in reduced voids, contributing to an enhanced green density. Conversely, lower values of the extrusion multiplier are associated with larger voids, ultimately leading to a lower green density. A similar trend in the weight density of samples printed with steel and binder has been reported in the FFF literature [45, 46].

### 3.2.3 Effect of nozzle speed

Three different nozzle speeds (20, 30, and 40 mm/s) were employed in this study. Fig 4(c) illustrates that the green density decreased as the nozzle speed increased. Lower nozzle speeds proved advantageous in achieving higher green density by effectively filling gaps during material deposition in the printing process. This slower speed promotes the extrusion of homogeneous materials, thereby minimizing the occurrence of voids (Fig. 8(a)). It is essential to note the considerable presence of metal particles in the material, a characteristic of extrusion-based 3D printing using MIM feedstocks. Traditional thermoplastic

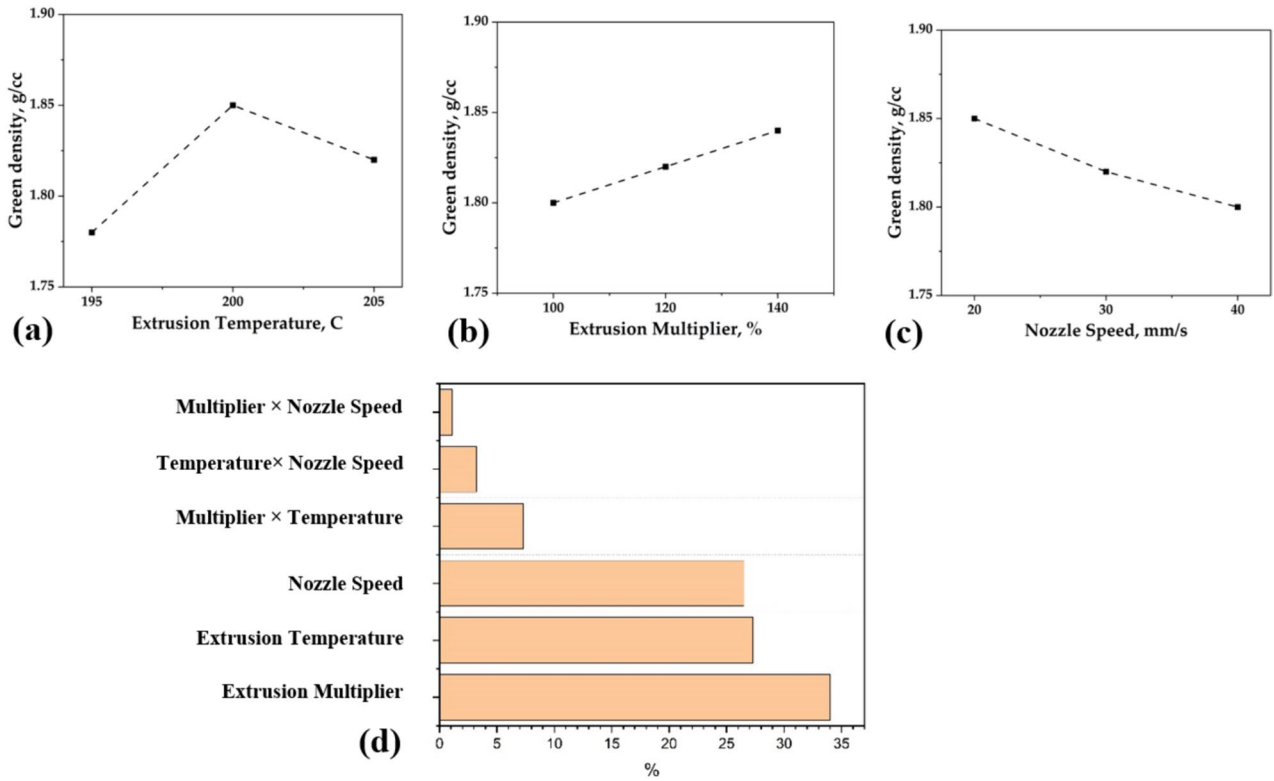


Fig. 4 Effect of (a) extrusion temperature, (b) extrusion multiplier and (c) nozzle speed on green density, and (d) percentage contribution of the parameters

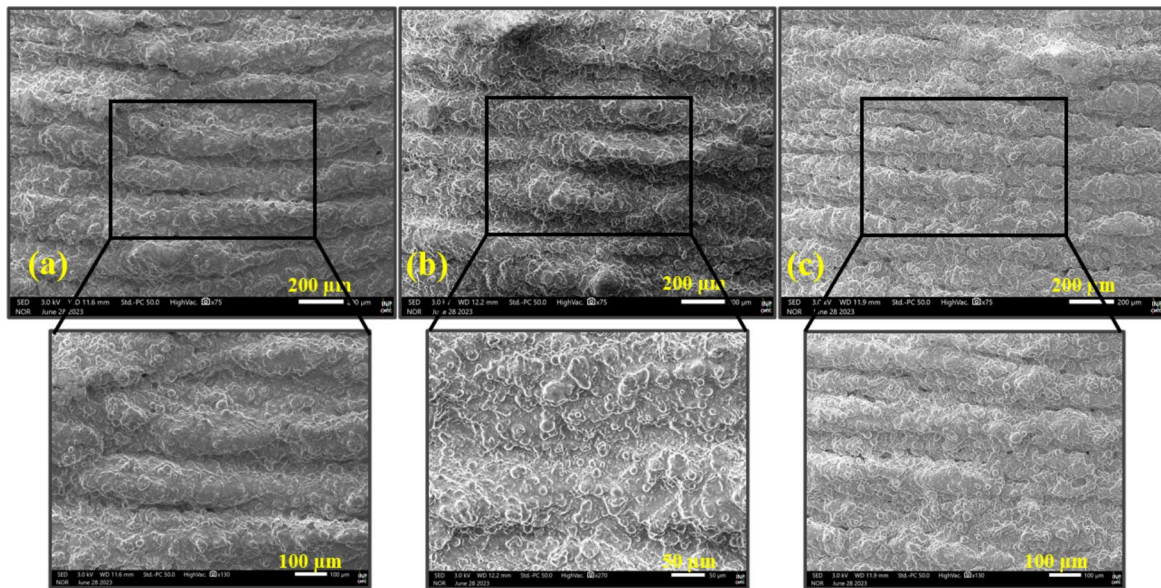


Fig. 5 SEM images of the sample printed with extrusion temperature of (a) 195, (b) 200, and (c) 205 °C

materials used in extrusion often exhibit ductility; however, the high loading of metal particles in the composite paste during extrusion may introduce brittleness. Heat transfer problems at high nozzle speeds can also change the local temperatures and influence feedstock rheology. At a high nozzle speed of 40 mm/s (Fig. 8(b)), the increased brittleness of the MIM feedstock may lead to breakage during the extrusion process, resulting in significant voids. This may explain the observed trend that an

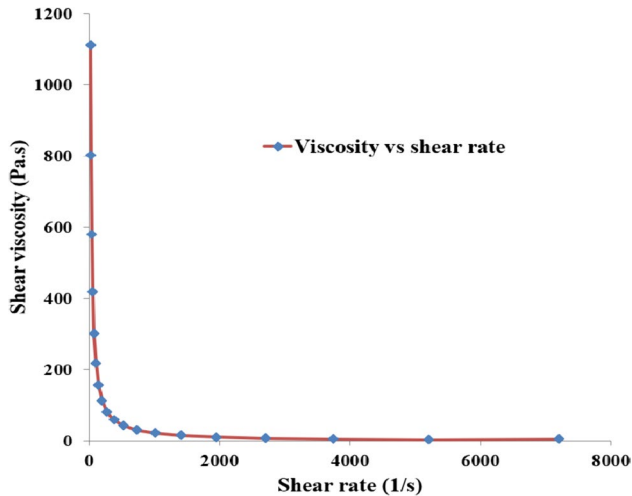
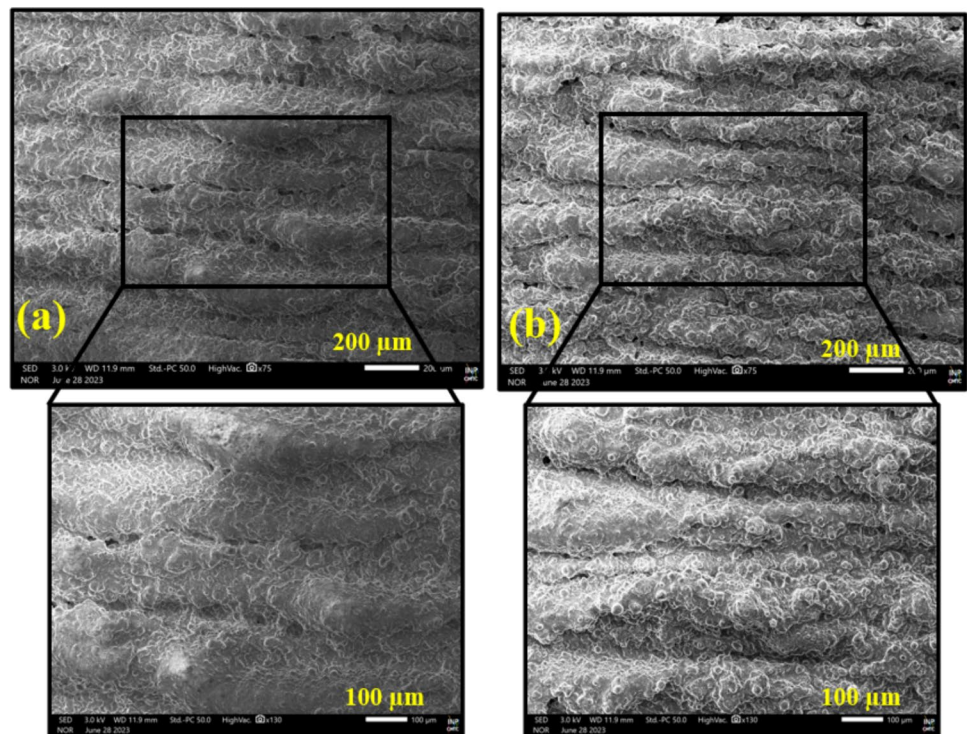


Fig. 6 Rheological behavior of feedstock at 200 °C

Fig. 7 SEM images of the sample printed with extrusion multiplier of (a) 100% and (b) 140%



increase in nozzle speed corresponds to larger voids and a subsequent decrease in green density.

### 3.3 Influence of printing parameters on surface roughness

Figure 9 shows the individual effects of the parameters on the surface roughness, providing insight into the percentage contribution of each factor. Throughout the experiments conducted in this study, the observed surface roughness was within the range of 9–14  $\mu\text{m}$ . The extrusion multiplier and nozzle speed emerged as the dominant parameters influencing surface roughness. No significant interactions were observed between the parameters that controlled surface roughness. Furthermore, the extrusion temperature exhibited a relatively modest impact on the surface roughness compared to the other parameters. However, an inverse trend is observed for the extrusion temperature at the central level. A detailed exploration of this trend is as follows.

#### 3.3.1 Effect of extrusion temperature

As shown in Fig. 9(a), the extrusion temperature had a limited influence on the surface roughness. An incremental increase in temperature from 195 °C to 200 °C was correlated with a reduction in surface roughness. However, upon further increasing the temperature to 205 °C, a subsequent increase in surface roughness was observed. This trend can be explained by the presence of fewer voids on the surface,

originating from the extrusion process at elevated temperatures. The increase in surface roughness at higher temperatures can be attributed to binder degradation, leading to the formation of larger voids that subsequently compromise the surface conditions and elevate surface roughness.

### 3.3.2 Effect of extrusion multiplier

The surface roughness decreased accordingly when the extrusion multiplier increased from 100 to 140%. Figures 7 and 5(b) (SEM of the sample with a 120% extrusion multiplier) illustrate this relationship, showing that an increasing extrusion multiplier enhances the uniformity of the extruded material deposition from 100 to 120%. The optimal surface condition was represented by the SEM images of the sample created with a 120% multiplier in Fig. 5(b), which showed a better surface finish and fewer voids. However, higher extrusion multiplier values increase the surface roughness above the 140% threshold because of the higher amount of extruded material deposited.

### 3.3.3 Effect of nozzle printing speed

The surface roughness increased with the nozzle printing speed. Lower nozzle speeds promoted more uniform

deposition of the extruded material, resulting in reduced surface roughness. Conversely, higher nozzle speeds create larger voids, culminating in a rough surface finish and elevated surface roughness values. These results are consistent with those in the literature on the FFF of thermoplastic and metal/binder mixture materials [40, 47].

### 3.4 Multi-objective optimization

A multi-objective optimization approach employing a genetic algorithm was utilized to minimize voids within the sample by maximizing the green density and enhancing the surface finish by minimizing roughness. The optimization was performed in SAS Institute's JMP 7 programs by considering regression Eqs. 1 and 2, constrained to the lower and higher levels of the parameters. The optimized parameters were identified as follows: extrusion temperature, 202 °C; extrusion multiplier, 140%; and printing speed, 20 mm/s. Predicted values for maximum green density and minimum surface roughness were  $1.9 \pm 0.03 \text{ g/cm}^3$  and  $7 \pm 0.9 \mu\text{m}$ , respectively. The experimental results using these optimized parameters yielded a green density of  $1.92 \text{ g/cm}^3$  and a surface roughness of  $7.3 \mu\text{m}$ , which closely aligned with the predicted values. A green density value of  $1.92 \text{ g/cm}^3$  corresponds to a relative density of 57% of the 6061 alloy particle

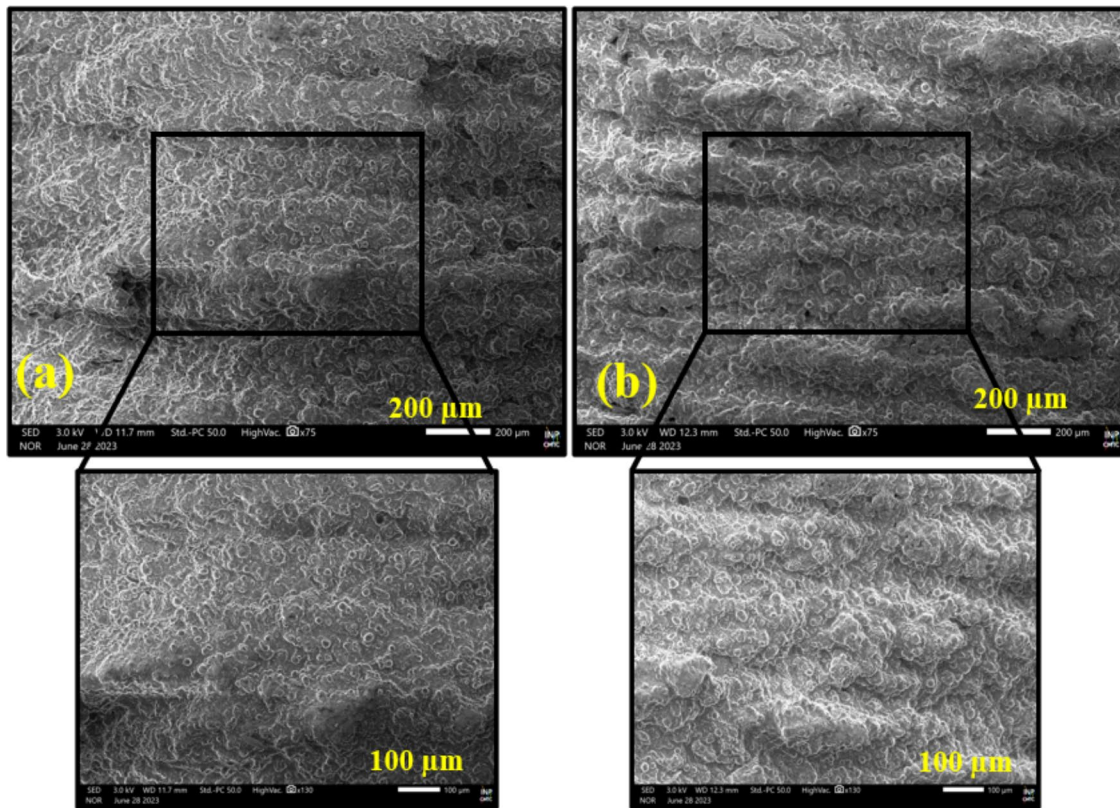
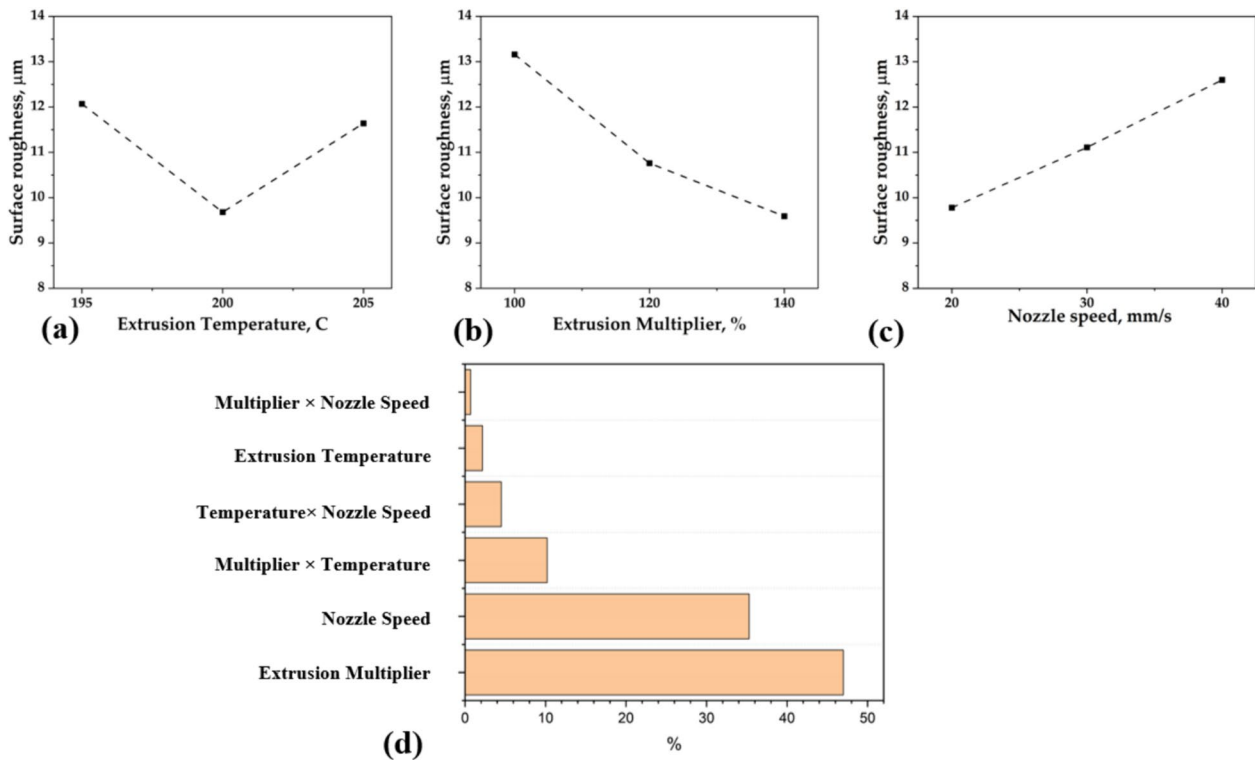


Fig. 8 SEM images of the sample printed with nozzle of (a) 20 mm/s and (b) 40 mm/s



**Fig. 9** Effect of (a) extrusion temperature, (b) extrusion multiplier and (c) nozzle speed on surface roughness, and (d) percentage contribution of the parameters

packing (excluding the 20 wt% binder), which is in line with the 6061 alloy content in the feedstock given by Ryer (58%). Figure 10 shows the SEM image, 2D line profile, and 3D surface profile of the sample fabricated using the optimized parameters. Notably, the surfaces of the fabricated parts exhibited no voids, and the uniform distribution of material between layers contributed to a smooth surface profile. This parameter optimization demonstrated its efficiency in producing defect-free products with enhanced surface quality through extrusion 3D printing.

### 3.5 Microtomography analysis

Microtomography characterization was conducted on a green sample printed with arbitrarily chosen non-optimized and optimized parameters to analyze the shape and size of the voids inside the fabricated green part samples. Figure 11 presents the raw horizontal and vertical cross-sectional images from the tomography scan, capturing three types of information. First, the black portions represent the voids formed during 3D printing. Second, the bright particles correspond to the phases containing heavy elements, such as Cu, Cr, or Fe, present in the Al6061 alloy. Third, a mixture of aluminum metal and binder is represented by

gray portions. The contrast and resolution obtained under our scanning conditions were not high enough to separate the binder and particles. During the 3D reconstruction of the tomography data (Fig. 12(a),(b)), the metal–binder mixture and voids were extracted as binary images for samples fabricated using unoptimized and optimized parameters.

For the sample fabricated with unoptimized parameters, the equivalent diameter range was approximately 6–245 μm, with an average diameter of approximately 25 μm. Large void channels were observed at a high magnification, as shown in Fig. 12(a). These large void channels could be attributed to the deviation of the printing parameters from the calculated optimum values. In contrast, the equivalent diameter range for the sample fabricated using the optimized parameters was approximately 6–39 μm, with an average diameter of approximately 7.2 μm. The void volume fraction of the optimized sample was calculated to be approximately 0.9%, compared with approximately 32% for the unoptimized sample. Tiny void channels were visible during void extraction at a high magnification (Fig. 12(b)). In addition, the heavy metal particles visible during the tomography scans were extracted. The volume fraction of these heavy metal particles was calculated as approximately 1.8%, with particle size ranging from 3.5 to 16.4 μm and an average

diameter of 8.34  $\mu\text{m}$ . These heavy metal particles had a spheroidal shape (Fig. 12(c)), with an average sphericity of 0.83.

### 3.6 Debinding and sintering

The green sample, printed using the optimized parameters, underwent a debinding process followed by sintering to achieve a dense aluminum part. The solvent debinding resulted in an approximate mass loss of 11 wt%. The remaining binder was removed during thermal debinding, corresponding to an approximate mass loss of 9 wt. %. Thermal debinding and sintering were performed consecutively, using a vertical dilatometer. Figure 13(a) illustrates the linear shrinkage of the sample sintered at a specified temperature. A significant amount of shrinkage is observed at the start of the temperature cycle during debinding. This initial shrinkage was attributed to the removal of the backbone binder from the material, which caused the sample to contract. At this stage, the polymer binder was completely removed. Swelling of the sample was observed when the temperature increased after reaching a plateau at 425  $^{\circ}\text{C}$ . A little shrinkage was noticed during the 630  $^{\circ}\text{C}$  plateau, corresponding to liquid-phase sintering, given the solidus temperature in the system ( $\sim 590$   $^{\circ}\text{C}$ ). The SEM images of the samples are shown (Fig. 13(b)). Two regions were identified for each sample: one region showed densification in the center, whereas the other was not completely densified. The experiments were conducted three times and yielded consistent results. A possible explanation is that the

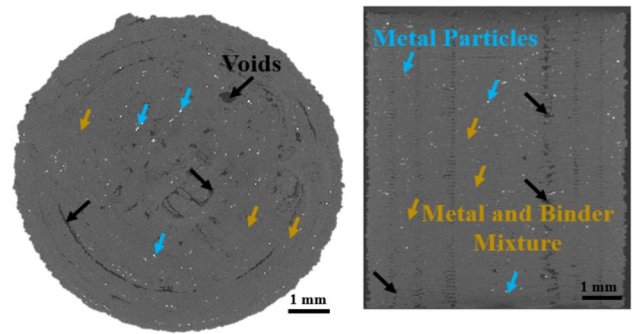


Fig. 11 Horizontal and vertical cross-section tomography images of a green part Al6061 sample with unoptimized printing parameters

oxygen partial pressure in the dilatometer was not low enough to enable the full reduction of the aluminum layer at the surface of the particles into AlN, a condition for the sintering of Al alloys, according to the literature [48]. Work is underway to better control the atmosphere and optimize the thermal cycle to improve densification during sintering.

## 4 Conclusions

This study aims to enhance the performance of extrusion 3D printing using Aluminum Al 6061 metal injection molding granules. The main goals were to minimize the surface roughness and maximize the green density.

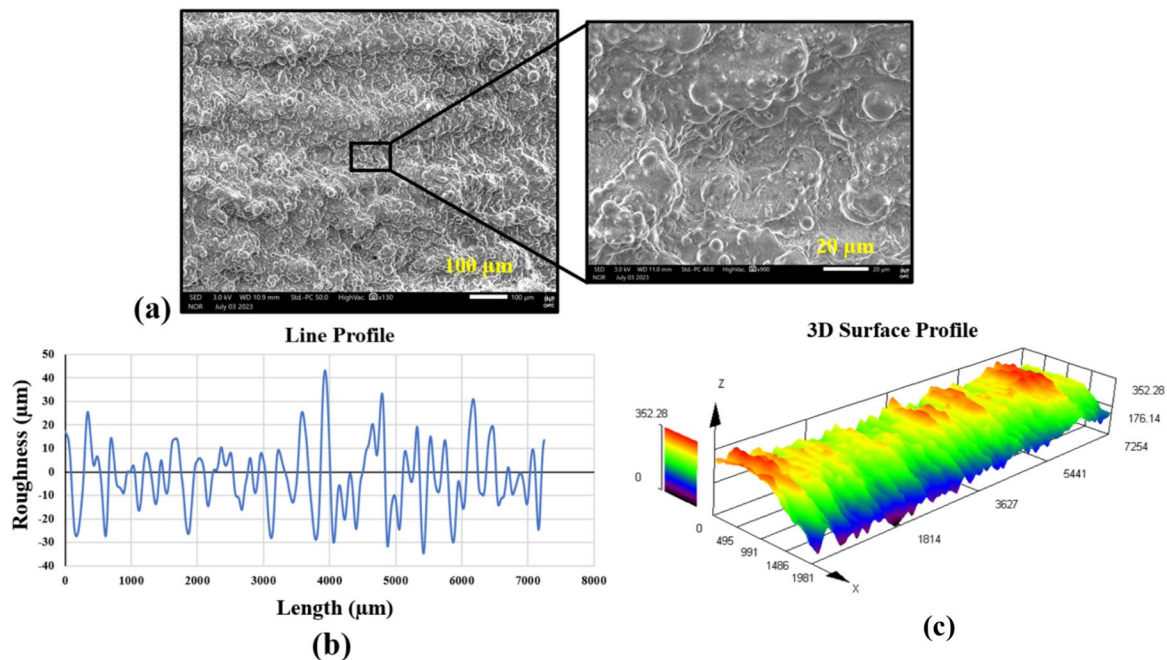
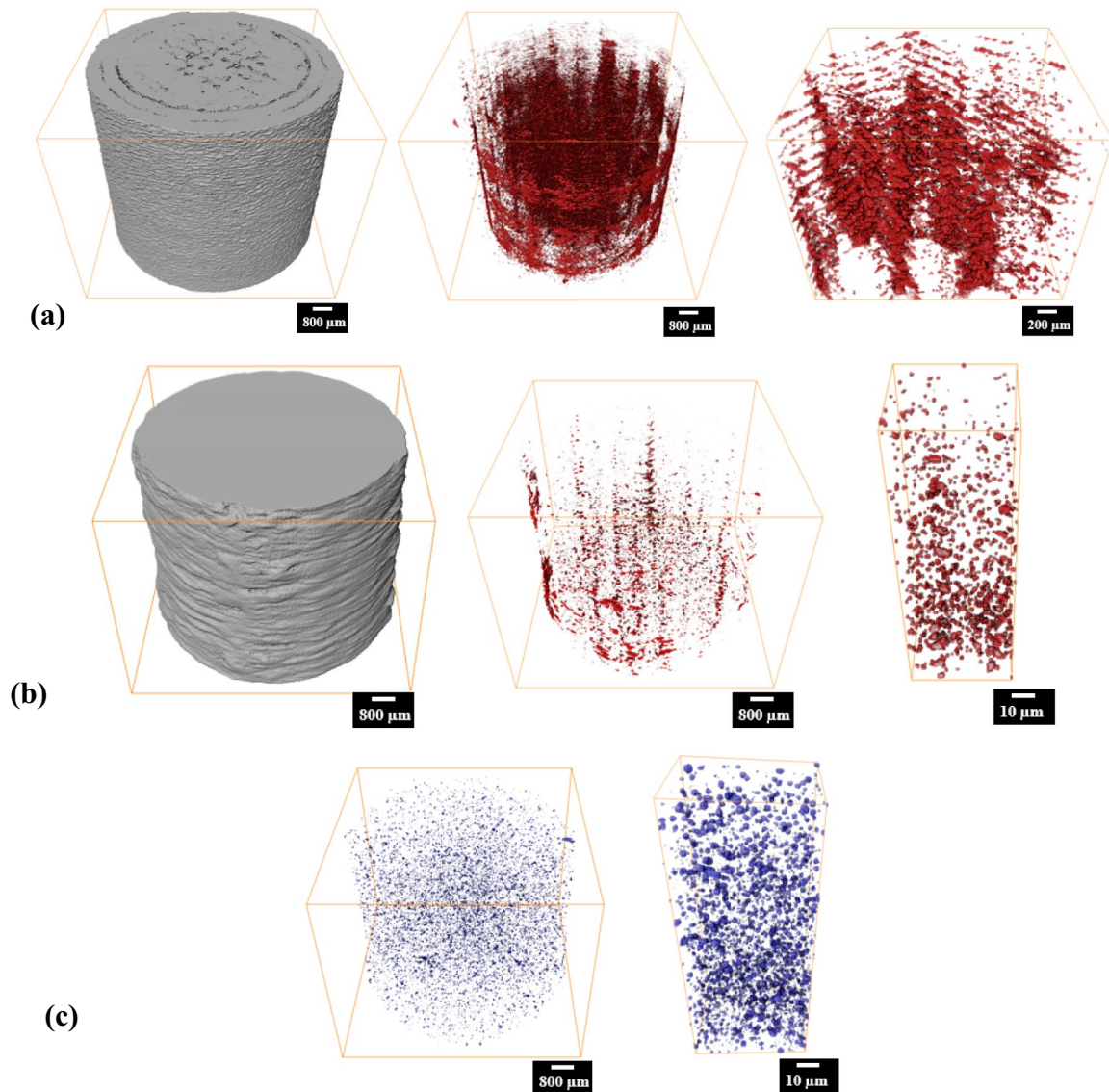


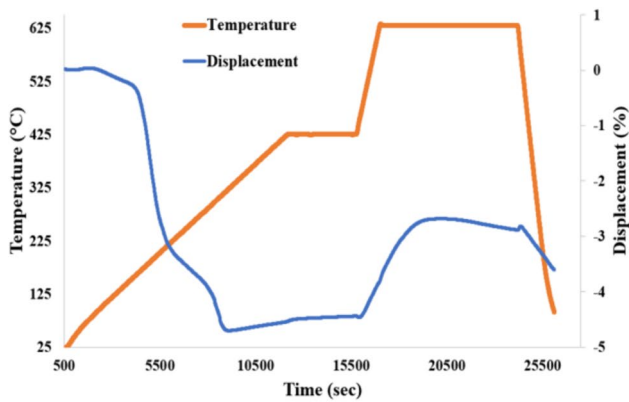
Fig. 10 (a) SEM picture (at lower and higher magnification), (b) line, and (c) 3D surface roughness profile of a sample manufactured at optimal settings



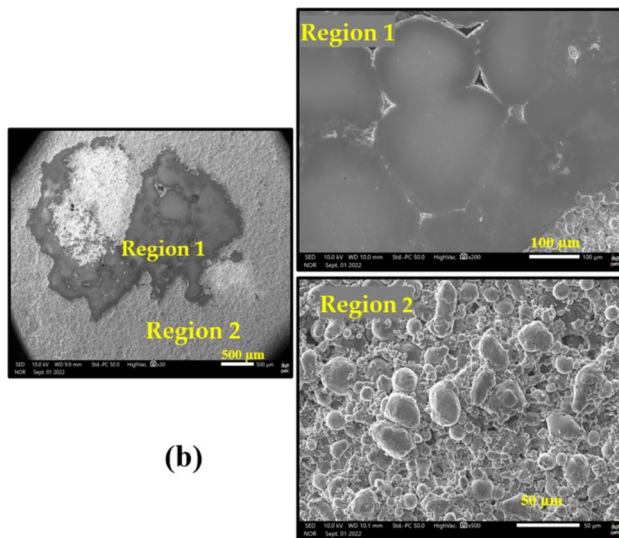
**Fig. 12:** 3D construction of the microtomography and extraction of voids for the samples fabricated with (a) unoptimized and (b) optimized parameters, and (c) extraction of heavy metal particles from the tomography of sample fabricated with optimized parameters

Quadratic statistical models were created using a design of experiments methodology to clarify the connections between the response variables (green density and surface roughness) and significant process parameters (extrusion temperature, extrusion flow rate multiplier, and nozzle printing speed). Based on empirical data, the following findings were obtained:

- By increasing the extrusion temperature between 195 and 205 °C, the green density first increased between 195 and 200 °C but then decreased between 200 °C and 205 °C. The optimum temperature corresponds to a compromise that ensures an appropriate viscosity for layer adhesion without binder deterioration. The green density exhibited a decline when the nozzle speed was increased from 20 to 40 mm/s. Conversely, an increase in the green density was noted with an increase in the extrusion multiplier from 100 to 140%. A higher extrusion multiplier increased the flow rate and minimized the extrusion voids, whereas a lower nozzle speed facilitated more uniform deposition, reducing voids.
- For similar reasons, the surface roughness exhibits a minimum value when increasing the temperature and decreases when increasing the extrusion multiplier or decreasing the nozzle speed.
- Multi-objective optimization yielded a green density of 1.92 g/cc and a surface roughness of 7 μm for an extrusion temperature of 202 °C, extrusion multiplier



(a)



(b)

**Fig. 13** (a) Dilatometric displacement curve corresponding to the sintering cycle and (b) SEM image of the sintered sample at different magnifications

of 140%, and nozzle speed of 20 mm/s. Microtomography of the samples printed with optimized and unoptimized parameters revealed the need to optimize the printing parameters to avoid porosity formation during the extrusion 3D printing stage.

- Chemical and thermal debinding were optimized for the complete elimination of the binder at 425 °C, and the 3D-printed sample was sintering at 630 °C under a nitrogen atmosphere. Densification by liquid-phase sintering is limited, and optimization of the sintering atmosphere and heating schedule is required to obtain samples with reduced porosity and acceptable mechanical properties.

The unknown binder composition was a limitation in this study for understanding the influence of the printing

parameters on the sample density and surface roughness. However, the optimized 3D printing extrusion technique shows promise for the fabrication of high-density aluminum components. Further refinement of the sintering process is necessary for optimal densification of the aluminum feedstock, and the fabrication of intricate shapes without any deformation during printing, debinding, and sintering is yet to be explored.

**Acknowledgements** The authors thank the Institute Carnot Energies du Futur for their financial support in this work (21U12—PRIMALU).

**Data availability** The data that support the findings of this study will be available from the corresponding author upon reasonable request.

## Declarations

**Conflict of interest** The authors declare no conflicts of interest. The funders had no role in the design of the study; in the collection, analyses, or interpretation of data; in the writing of the manuscript; or in the decision to publish the results.

## References

1. J.R. Davis, *Stainless steels*, ASM international, 1994.
2. Michi RA, Plotkowski A, Shyam A, Dehoff RR, Babu SS (2022) Towards high-temperature applications of aluminium alloys enabled by additive manufacturing. *Int Mater Rev* 67:298–345. <https://doi.org/10.1080/09506608.2021.1951580>
3. Georgantzia E, Gkantou M, Kamaris GS (2021) Aluminium alloys as structural material: a review of research. *Eng Struct*. <https://doi.org/10.1016/j.engstruct.2020.111372>
4. Omiyale BO, Olugbade TO, Abioye TE, Farayibi PK (2022) Wire arc additive manufacturing of aluminium alloys for aerospace and automotive applications: a review. *Mater Sci Technol (United Kingdom)* 38:391–408. <https://doi.org/10.1080/02670836.2022.2045549>
5. Yang J, Oliveira JP, Li Y, Tan C, Gao C, Zhao Y, Yu Z (2022) Laser techniques for dissimilar joining of aluminum alloys to steels: a critical review. *J Mater Process Technol*. <https://doi.org/10.1016/j.jmatprotec.2021.117443>
6. Chak V, Chattopadhyay H, Dora TL (2020) A review on fabrication methods, reinforcements and mechanical properties of aluminum matrix composites. *J Manuf Process* 56:1059–1074. <https://doi.org/10.1016/j.jmapro.2020.05.042>
7. J. Joys, (2014) *Aluminium MIM: New advanced powders and feedstocks achieve higher densities*, Powder Injection Moulding International
8. J.F. Nie, A.J. Morton, B.C. Muddle, K. Nishiyabu, S. Matsuzaki, M. Ishida, S. Tanaka, H. Nagai 2004 Development of Porous Aluminium by Metal Injection Moulding
9. Singh N, Singh G (2021) Advances in polymers for bio-additive manufacturing: a state of art review. *J Manuf Process* 72:439–457. <https://doi.org/10.1016/j.jmapro.2021.10.045>
10. Singh S, Singh G, Prakash C, Ramakrishna S (2020) Current status and future directions of fused filament fabrication. *J Manuf Process* 55:288–306. <https://doi.org/10.1016/j.jmapro.2020.04.049>

11. Wong KV, Hernandez A (2012) A review of additive manufacturing, international scholarly research. *Network* 2012:1–10. <https://doi.org/10.5402/2012/208760>
12. Tucho WM, Hansen V (2019) Characterization of SLM-fabricated Inconel 718 after solid solution and precipitation hardening heat treatments. *J Mater Sci* 54:823–839. <https://doi.org/10.1007/s10853-018-2851-x>
13. Jeong W, Kwon Y, Kim D (2019) Three-dimensional printing of tungsten structures by directed energy deposition. *Mater Manuf Processes* 34:986–992. <https://doi.org/10.1080/10426914.2019.1594253>
14. Farzaneh A, Khorasani M, Farabi E, Gibson I, Leary M, Ghaseini AH, Rolfe B (2022) Sandwich structure printing of Ti-Ni-Ti by directed energy deposition. *Virtual Phys Prototyp* 17:1006–1030. <https://doi.org/10.1080/17452759.2022.2096647>
15. Aboulkhair NT, Simonelli M, Parry L, Ashcroft I, Tuck C, Hague R (2019) 3D printing of Aluminium alloys: Additive Manufacturing of Aluminium alloys using selective laser melting. *Prog Mater Sci*. <https://doi.org/10.1016/j.pmatsci.2019.100578>
16. Wang CG, Zhu JX, Wang GW, Qin Y, Sun MY, Yang JL, Shen XF, Huang SK (2022) Effect of building orientation and heat treatment on the anisotropic tensile properties of AlSi10Mg fabricated by selective laser melting. *J Alloys Compd*. <https://doi.org/10.1016/j.jallcom.2021.162665>
17. Yang H, Zhang Y, Wang J, Liu Z, Liu C, Ji S (2021) Additive manufacturing of a high strength Al-5Mg2Si-2Mg alloy: microstructure and mechanical properties. *J Mater Sci Technol* 91:215–223. <https://doi.org/10.1016/j.jmst.2021.02.048>
18. Martin JH, Yahata BD, Hundley JM, Mayer JA, Schaedler TA, Pollock TM (2017) 3D printing of high-strength aluminium alloys. *Nature* 549:365–369. <https://doi.org/10.1038/nature23894>
19. Ziaee M, Crane NB (2019) Binder jetting: a review of process, materials, and methods. *Addit Manuf* 28:781–801. <https://doi.org/10.1016/j.addma.2019.05.031>
20. Miyajima H, Ma D, Atwater MA, Darling KA, Hammond VH, Williams CB (2020) Binder jetting additive manufacturing of copper foam structures. *Addit Manuf*. <https://doi.org/10.1016/j.addma.2019.100960>
21. Tosto C, Tirillò J, Sarasini F, Cicala G (2021) Hybrid metal/polymer filaments for fused filament fabrication (FFF) to print metal parts. *App Sci (Switzerland)* 11:1. <https://doi.org/10.3390/app11041444>
22. Abel J, Scheithauer U, Janics T, Hampel S, Cano S, Müller-Köhn A, Günther A, Kukla C, Moritz T (2019) Fused filament fabrication (FFF) of metal-ceramic components. *J Visualized Exp*. <https://doi.org/10.3791/57693>
23. Thompson Y, Zissel K, Förner A, Gonzalez-Gutierrez J, Kukla C, Neumeier S, Felfel P (2022) Metal fused filament fabrication of the nickel-base superalloy IN 718. *J Mater Sci* 57:9541–9555. <https://doi.org/10.1007/s10853-022-06937-y>
24. C. Burkhardt, P. Freigassner, O. Weber, P. Imgrund, S. Hampel (2016) Fused filament fabrication (FFF) of 316L green parts for the MIM process, World PM 2016 Congress and Exhibition 1
25. Singh G, Missiaen J-M, Didier Bouvard J-M, Chaix (2021) Copper additive manufacturing using MIM feedstock: adjustment of printing, debinding, and sintering parameters for processing dense and defectless parts. *Intl J Adv Manuf Technol* 115:449–462. <https://doi.org/10.1007/s00170-021-07188-y/Published>
26. Singh G, Missiaen JM, Bouvard D, Chaix JM (2021) Additive manufacturing of 17–4 PH steel using metal injection molding feedstock: analysis of 3D extrusion printing, debinding and sintering. *Addit Manuf*. <https://doi.org/10.1016/j.addma.2021.102287>
27. D. Jiang, F. Ning (2023). Bi-metal structures fabricated by extrusion-based sintering-assisted additive manufacturing. *J Manuf Process*
28. Mamatha S, Biswas P, Ramavath P, Das D, Johnson R (2018) 3D printing of complex shaped alumina parts. *Ceram Int* 44:19278–19281. <https://doi.org/10.1016/j.ceramint.2018.07.153>
29. C. Kenel, J.P. Sessege, N.R. Geisendorfer, R.N. Shah, R. Spolenak, D.C. Dunand, D. Dunand (2020) 3D-printed Tungsten Sheet-Gyroids via Reduction and Sintering of Extruded WO3-Nanopowder Inks.
30. M. Zanon, A. Müller, J.R. Croteau, N. Murphy, J. Workman, ; Tom Pelletiers, Metal Binder-jetting Of Aluminium-based Alloys, n.d.
31. Yamaguchi D, Oya N (2023) X-ray observation study of the influence of binder deposition on sintering process of aluminum binder jetting. *Int J Adv Manuf Technol* 128:1981–1990. <https://doi.org/10.1007/s00170-023-12058-w>
32. Malone L (2022) Additive manufacturing of aluminum alloy by metal fused filament fabrication (MF3). *Univ Louisville*. <https://doi.org/10.18297/etd/3927>
33. Galindo E, Maric M, Postigo AA, Walker A, Conlon M, Azari K, Brochu M (2023) Metal fused filament fabrication of AlSi10Mg aluminum alloy †. *Eng Proc*. <https://doi.org/10.3390/engproc2023043037>
34. Ding H, Zeng C, Raush J, Momeni K, Guo S (2022) Developing fused deposition modeling additive manufacturing processing strategies for aluminum alloy 7075: sample preparation and metallographic characterization. *Materials*. <https://doi.org/10.3390/ma15041340>
35. Momeni V, Shahroodi Z, Gonzalez-Gutierrez J, Hentschel L, Duretek I, Schuschnigg S, Kukla C, Holzer C (2023) Effects of different polypropylene (PP)-backbones in aluminium feedstock for fused filament fabrication (FFF). *Polymers (Basel)*. <https://doi.org/10.3390/polym15143007>
36. Tang S, Yang Y, Yang L, Fan Z (2022) A green extrusion-based 3D printing of hierarchically porous aluminum. *Powder Technol*. <https://doi.org/10.1016/j.powtec.2022.117198>
37. Dayam S, Tandon P, Priyadarshi S (2022) Development of paste extrusion-based metal additive manufacturing process. *Rapid Prototyp J* 28:1920–1932. <https://doi.org/10.1108/RPJ-05-2021-0118>
38. Manoel J, Netto J, Idogava HT, Luiz EF, Santos Z, De C, Silveira P, Romio JLA (2021) Screw-assisted 3D printing with granulated materials: a systematic review. *Int J Adv Manuf Technol* 115:2711–2727. <https://doi.org/10.1007/s00170-021-07365-z/Published>
39. Singh G, Missiaen J, Bouvard D, Chaix J (2021) Copper additive manufacturing using MIM feedstock : adjustment of printing, debinding, and sintering parameters for processing dense and defectless parts. *Int J Adv Manuf Technol*. <https://doi.org/10.1007/s00170-021-07188-y>
40. Singh G, Missiaen JM, Bouvard D, Chaix JM (2021) Copper extrusion 3D printing using metal injection moulding feedstock: Analysis of process parameters for green density and surface roughness optimization. *Addit Manuf*. <https://doi.org/10.1016/j.addma.2020.101778>
41. Kent D, Qian M, Schaffer GB (2010) Formation of aluminium nitride during sintering of powder injection moulded aluminium. *Powder Metall* 53:118–124. <https://doi.org/10.1179/003258909X12523294330154>
42. Geometrical product specifications (GPS) — Surface texture: Profile, ISO 21920–2:2021 (n.d.).
43. Corder RD, Chen YJ, Pibulchinda P, Youngblood JP, Ardekani AM, Erk KA (2023) Rheology of 3D printable ceramic suspensions: effects of non-adsorbing polymer on discontinuous shear thickening. *Soft Matter* 19:882–891. <https://doi.org/10.1039/d2sm01396g>
44. Luo Y, Sun W, Bao M, Zhu X, Ning C, Zhang W, Li Y, Zhang X (2023) Process fundamentals and quality investigation in extrusion 3D printing of shear thinning materials: extrusion process

- based on Nishihara model. *Int J Adv Manuf Technol* 124:245–264. <https://doi.org/10.1007/s00170-022-10506-7>
45. Godec D, Cano S, Holzer C, Gonzalez-Gutierrez J (2020) Optimization of the 3D printing parameters for tensile properties of specimens produced by fused filament fabrication of 17–4PH stainless steel. *Materials*. <https://doi.org/10.3390/ma13030774>
46. J. Gonzalez-Gutierrez, D. Godec, C. Kukla, T. Schlauf, C. Burkhardt, C. Holzer, Shaping (2017) Debinding and sintering of steel components via fused filament fabrication, 16th International Scientific Conference on Production Engineering - CIM2017
47. Radhwan H, Shayfull Z, Farizuan MR, Effendi MSM, Irfan AR (2019) Optimization parameter effects on the quality surface finish of the three-dimensional printing (3D-printing) fused deposition modeling (FDM) using RSM. *AIP Conf Proc*. <https://doi.org/10.1063/1.5118163>
48. J. Kuzmanovic, H. Danninger, C. Gierl-Mayer, A. Nenning, A. Avakemian (2015) Interstitial Effects during Sintering of Injection Moulded Al Base Alloys, in: *European Powder Metallurgy Association*, p. 6.

**Publisher's Note** Springer Nature remains neutral with regard to jurisdictional claims in published maps and institutional affiliations.

Springer Nature or its licensor (e.g. a society or other partner) holds exclusive rights to this article under a publishing agreement with the author(s) or other rightsholder(s); author self-archiving of the accepted manuscript version of this article is solely governed by the terms of such publishing agreement and applicable law.